A case study on the correction of atmosphere-induced phase disturbances for SAR tomography in mountainous areas

Muhammad Adnan Siddique[1], Tazio Strozzi[3], Irena Hajnsek[1,2], Othmar Frey[1,3]

[1]Chair of Earth Observation & Remote Sensing, ETH Zurich, Switzerland, Email: siddique@ifu.baug.ethz.ch
[2]Microwaves & Radar Institute, Oberpfaffenhofen, German Aerospace Center – DLR, Germany
[3]GAMMA Remote Sensing AG, Gümligen, Switzerland

Abstract

The estimation of the atmosphere-induced phase delay variations is often more involved in mountainous areas due to strong spatial variations of the local atmospheric conditions and propagation paths through the troposphere. Height-dependent phase delay variation owing to vertical stratification of the atmosphere within the same range-azimuth resolution cell cannot be ignored. We propose a regression kriging-based data-driven method whereby phase corrections are applied for differential tomographic focusing at each 3D point of interest along the elevation axis. Experiments are performed on an interferometric stack comprising 32 Cosmo-SkyMed stripmap images acquired between 2008-2013 over the Matter Valley in the Swiss Alps.

1 Introduction

Remote sensing with spaceborne synthetic aperture radar (SAR) involves two-way propagation of the EM-wave through the atmosphere which acts as a refractive medium. Since the optical path traversed by the waves in troposphere is longer than the geometric path, additional phase delays are accumulated. The refractivity is mainly governed by temperature, pressure and water vapor, which vary in time and space [1]. Consequently, the refractivity changes over the scene as well as from one pass to the next, incurring variable phase delays which in general do not cancel out in interferogram formation leaving behind a phase footprint which is typically a nuisance. In case of tomography, it acts as a disturbance in focusing the scatterers in 3D [2, 3]. Consequently, layovers of potentially coherent scatterers may remain unresolved, and errors may also occur in differential tomography-based retrieval of deformation parameters [4]. Therefore, the interferometric data stack requires a precise phase calibration prior to tomographic inversion.

The role of the atmosphere is generally modeled in two aspects. Firstly, the 3D heterogeneities in refractivity caused by turbulent mixing; secondly, a general decrease in refractivity with increasing altitude under normal atmospheric conditions, considering the lower troposphere to be a vertically stratified medium comprising thin layers that are horizontally homogeneous. Contrary to regions of flat topography where only turbulent mixing effects are relevant, in alpine regions both the turbulent mixing and vertical stratification contribute to variable phase delays [1]. Therefore, the atmospheric correction needed for a given scatterer may be very different from another

situated at a different altitude, notwithstanding that they maybe in the same range-azimuth pixel (i.e., in a layover). Hence, a single correction for a range-azimuth pixel does not suffice. Instead, the atmospheric phases have to be estimated and compensated for within the tomographic focusing at each point of interest along the elevation axis.

2 Methods

2.1 SAR Tomography

Modeling each scatterer as a deterministic (point-like) target, and considering a coregistered and phase calibrated interferometric stack, the mathematical model for differential SAR tomography can be written as [5, 6, 4]:

$$y_m = \iint\limits_{\mathcal{I}_s \mathcal{I}_v} \alpha (s, v) \exp \left[-j\varphi_m (s, v) \right] \mathrm{d}s \mathrm{d}v \qquad (1)$$

where y_m is the SLC value for a given range-azimuth pixel from the mth layer of the stack, where $m = 0, 1, \ldots, M - 1$. The target complex reflectivity, $\alpha (s, v)$ is a function of the scatter elevation s and linear deformation velocity v. $\mathcal{I}_s$ and $\mathcal{I}_v$ represent the support of s and v, respectively. The interferometric phase is modeled as follows:

$$\varphi_m (s, \nu) = 2k \left[\triangle r_m (s) + vt_m \right] \qquad (2)$$

where t_m is the mth temporal baseline and $\triangle r_m (s)$ is the sensor-to-target geometric path-length difference for the interferometric pair:

$$\triangle r_n (s) \approx \frac{s^2}{2 \left(r_0 - b_n^{\parallel} \right)} - \frac{b_n^{\perp} s}{r_0 - b_n^{\parallel}}. \qquad (3)$$

where $b_m^{\perp}$ and $b_m^{\parallel}$ are the orthogonal and parallel components of the m$^{\text{th}}$ spatial baseline, respectively. To model atmospheric phases in differential tomography, the mathematical model in eq. (1) is rewritten as:

$$y_m^{pd} = \iint\limits_{\mathcal{I}_s \mathcal{I}_v} \alpha(s,v) \exp\left[j\psi_m(s)\right] \exp\left[-j\varphi_m(s,v)\right] \mathrm{d}s\mathrm{d}v$$

(4)

where $\psi_m(s)$ is the elevation-dependent atmosphere-induced interferometric phase due to refractivity change between the acquisitions forming the mth interferogram, and y_m^{pd} is the SAR signal observed in the presence of these atmospheric phases. It is assumed here that the refractivity changes are uncorrelated with the temporal baselines.
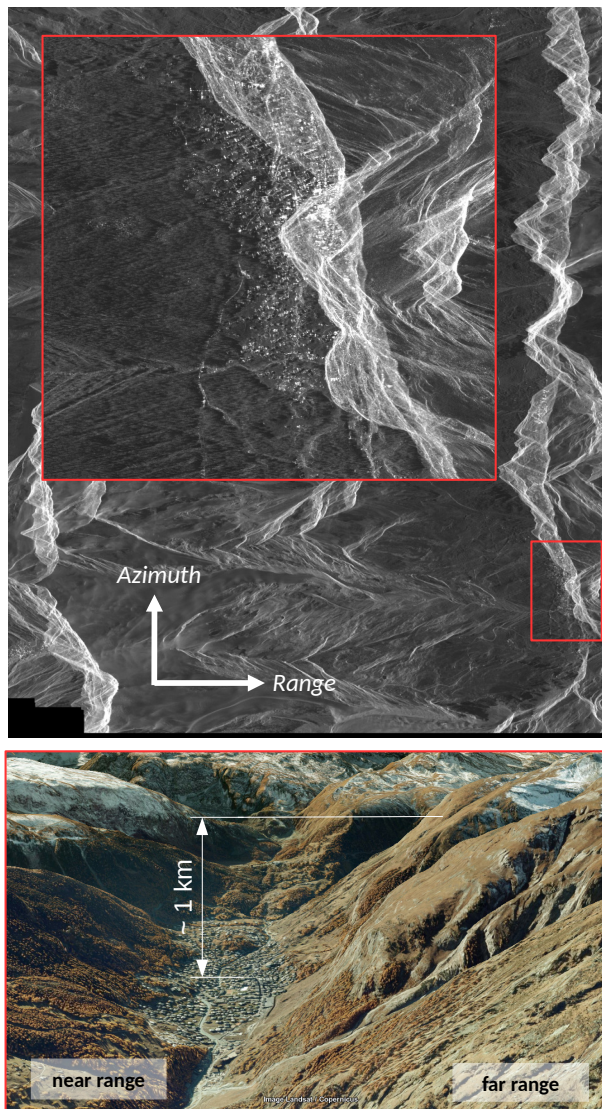

Figure 1: Top: SAR average intensity for 32 Cosmo-SkyMed acquisitions over Matter Valley in the Swiss Alps. The region of interest (ROI) for tomographic analysis is Zermatt village and surroundings, as indicated with the red-colored rectangle. Below: An optical perspective of the ROI, courtesy Google Earth.

2.2 PSI Processing

We perform persistent scatterer interferometric (PSI) processing using the IPTA [7] toolbox. The preprocessing includes selection of a reference acquisition and coregistration of the data stack using an external digital elevation model (DEM) [8]. An iterative regression-based strategy is employed to identify a set of persistent scatterers (PS) exhibiting good quality (in terms of low dispersion of the residual phase). The PSI solution obtained after several iterations comprises the estimated residual height of the PS, the average deformation velocity and the atmospheric phases. A linear model of the unwrapped atmospheric phases with respect to height is implemented within the PSI processing to model vertical stratification [9, 10]. The atmospheric phases thus computed for the PS are then interpolated using regression-kriging to obtain estimates of the atmospheric phase at different heights and spatial coordinates prior to tomographic focusing, as explained next.

2.3 Regression-Kriging

The PS identified in the interferometric processing are geocoded. We consider the atmospheric phases estimated for the PS as samples of the physical 3D spread of the atmospheric phase signal over the scene. Considering the possibility of lateral variations besides vertical stratification effects, we model the unwrapped atmospheric phases for a given interferometric layer from the stack with the following multiple linear regression model:

$$\psi(\boldsymbol{x}) = \begin{bmatrix} 1 & x_e & x_n & h \end{bmatrix}\boldsymbol{\beta} + \varepsilon(\boldsymbol{x})$$

(5)

where $\boldsymbol{x} \triangleq (x_e, x_n, h) = \mathbb{T}\{r, a, s\}$ represents a general 3D location in map geometry in terms of easting, x_e, northing, x_n and height, h, where $\mathbb{T}\{\boldsymbol{\cdot}\}$ is the geocoding transformation applied on a range-azimuth-elevation tuple, (r, a, s). The vector $\boldsymbol{\beta}$ contains the regression coefficients. The atmospheric phases computed for the PS are regressed on their 3D map coordinates for each interferometric layer. The linear dependence on map coordinates attempts to extract 'trends' in the atmospheric phases, lateral as well as vertical. Using the estimated residuals, $\hat{\varepsilon}(\boldsymbol{x})$ and assuming second-order stationarity and isotropy (direction-independence of the semivariance of the residue), we compute the sample variogram as follows [11, 12, 13]:

$$\hat{\gamma}(\tilde{\ell}_j) = \frac{1}{2\mathcal{N}(\ell)}\sum_{i=1}^{\mathcal{N}(\ell)} \{\hat{\varepsilon}(\boldsymbol{x}_i) - \hat{\varepsilon}(\boldsymbol{x}_i + \hat{\boldsymbol{\iota}}\ell)\}^2, \ \ \forall l \in \tilde{\ell}_j$$

(6)

where $\hat{\varepsilon}(\boldsymbol{x}_i)$ is the residue for the ith PS, $\hat{\varepsilon}(\boldsymbol{x}_i + \hat{\boldsymbol{\iota}}\ell)$ is the residue for a PS that is located such that the radial distance between the location pair $\{(\boldsymbol{x}_i), (\boldsymbol{x}_i + \hat{\boldsymbol{\iota}}\ell)\}$ is within the given distance interval, $\tilde{\ell}_j$ and $\mathcal{N}(\ell)$ is the number of such paired comparisons. $\hat{\boldsymbol{\iota}}$ represents a unit vector in any direction. The subscript j indicates the index over the distance intervals used to compute the sample variogram.

2

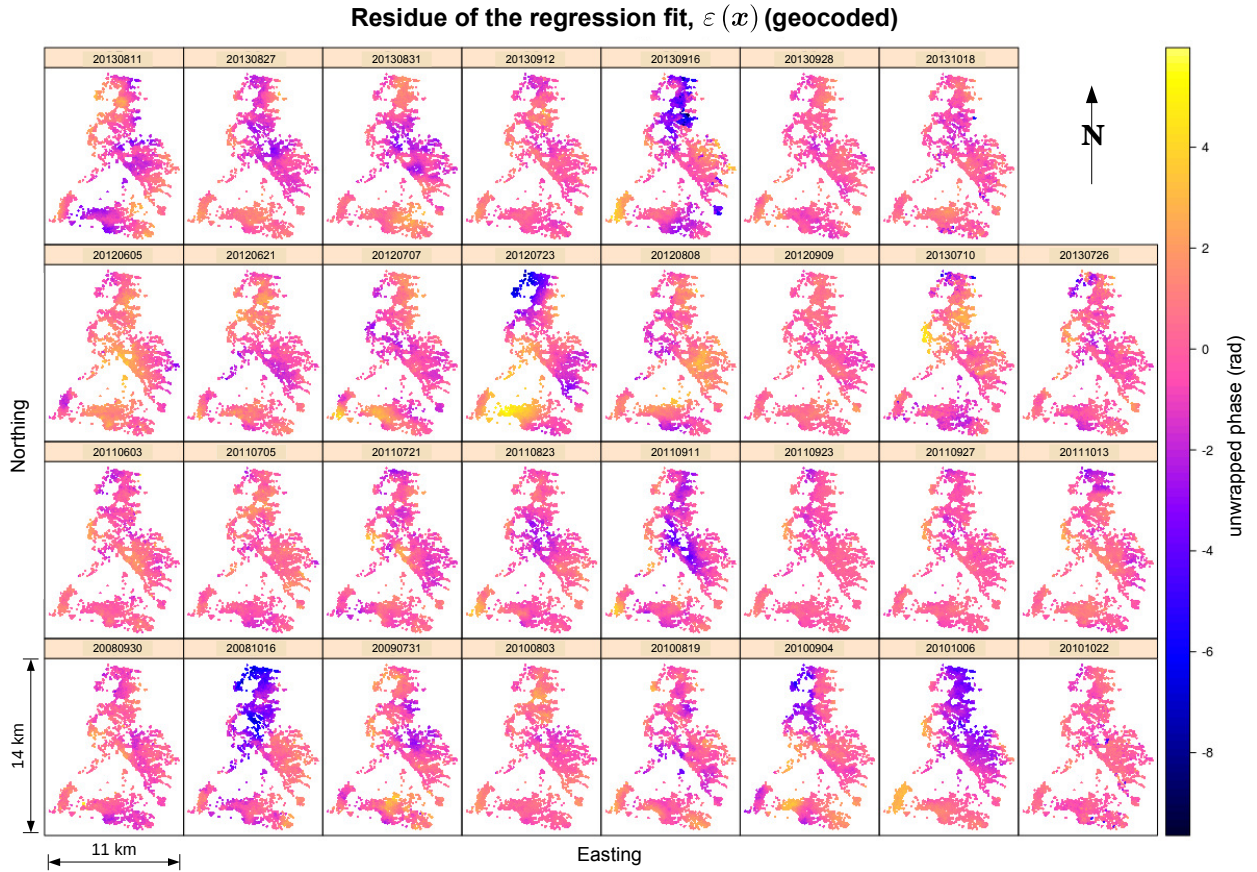**Residue of the regression fit, $\varepsilon\left(x\right)$ (geocoded)**

Figure 2: Geocoded residue of the multiple linear regression fit of the unwrapped atmospheric phases against easting, northing and height. The title of each sub-figures indicates the date of the SAR acquisition in YYYYMMDD format, whose phase is referenced to the acquisition on 20100920.

The regression-kriging aka universal kriging-based best linear unbiased predictor (BLUP) of the atmospheric phase at any 3D location $\boldsymbol{x}_0$ is [13, 11]:

$$\hat{\psi}(\boldsymbol{x}_0) = \mathbf{x}_0^T \hat{\boldsymbol{\beta}} + \mathbf{v}^T V^{-1}\left(\boldsymbol{\Psi} - \mathbf{X}\hat{\boldsymbol{\beta}}\right) \qquad (7)$$

where $\mathbf{X}$ is the design matrix and $\boldsymbol{\Psi}$ is the vector of the atmospheric phases at PS locations:

$$\mathbf{X} = \begin{bmatrix} \mathbf{x}_1^T \\ \mathbf{x}_2^T \\ \vdots \\ \mathbf{x}_{N_{\mathrm{ps}}}^T \end{bmatrix}, \quad \boldsymbol{\Psi} = \begin{bmatrix} \psi\left(\boldsymbol{x}_1\right) \\ \psi\left(\boldsymbol{x}_2\right) \\ \vdots \\ \psi\left(\boldsymbol{x}_{N_{\mathrm{ps}}}\right) \end{bmatrix}. \qquad (8)$$

$\mathbf{V}$ is the data covariance matrix for the PS locations, and $\mathbf{v}$ is the covariance vector corresponding to the location $\boldsymbol{x_0}$. They are computed after fitting the sample variogram with a parametric model, and exploiting the following relationship among them under the assumption of second order stationarity:

$$\mathrm{V}(\ell) = \mathrm{V}(0) - \gamma(\ell). \qquad (9)$$

N_{ps} is the number of PS used for kriging setup. The regression coefficients can be estimated with generalized least squares [11]:

$$\hat{\boldsymbol{\beta}} = (\mathbf{X}^T \mathbf{V}^{-1} \mathbf{X})^{-1} \mathbf{X}^T \mathbf{V}^{-1} \boldsymbol{\Psi}. \qquad (10)$$

2.4 Tomographic focusing

Considering M acquisitions, the observed SAR signal vector for a given range-azimuth pixel (r, a) is

$$\mathbf{y}^{pd} = \begin{bmatrix} y_0^{pd} & y_1^{pd} & \cdots & y_{M-1}^{pd} \end{bmatrix}^T. \qquad (11)$$

The observed elevation and deformation extents, $\mathcal{I}_s$ and $\mathcal{I}_v$, respectively, are discretized. Inverting the differential tomographic model in eq. (4), the 2D scatterer reflectivity at the discrete pair (s_k, v_l) is focused using single-look beamforming (BF) as follows:

$$\hat{\alpha}\left(s_k, v_l\right) = \frac{1}{M} \mathbf{a}^H\left(s_k, v_l\right) \mathbf{y}^{pd}. \qquad (12)$$

The steering vector $\mathbf{a}\left(s_k, v_l\right)$ is set up such that atmospheric phase correction is incorporated within the tomographic focusing at each discrete point of interest along the elevation axis, as shown below:

$$\mathbf{a}\left(s_k, v_l\right) =$$
$$\begin{bmatrix} \exp\left[-j\left\{\varphi_0\left(s_k, v_l\right) + \hat{\psi}_0\left(\mathbb{T}\left\{r, a, s\right\}\right)\right\}\right] \\ \exp\left[-j\left\{\varphi_1\left(s_k, v_l\right) + \hat{\psi}_1\left(\mathbb{T}\left\{r, a, s\right\}\right)\right\}\right] \\ \vdots \\ \exp\left[-j\left\{\varphi_{M-1}\left(s_k, v_l\right) + \hat{\psi}_{M-1}\left(\mathbb{T}\left\{r, a, s\right\}\right)\right\}\right] \end{bmatrix}. \qquad (13)$$
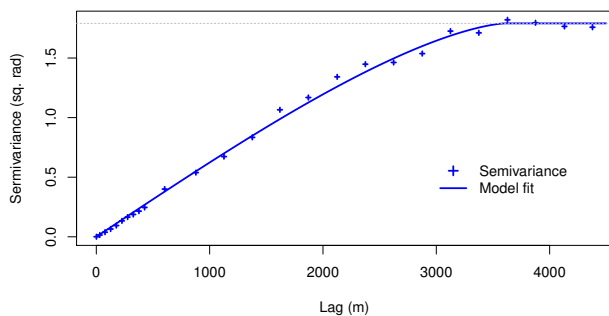
3

Figure 3: Sample variogram and a parametric model fit (circular) for the residue of the regression fit (eq. 5) for an example interferometric layer (20130811).

For the estimation of the unknown scatterer elevation and deformation, and single and double scatterer detection, we apply BF-based maximizations under the *sequential generalized likelihood ratio test with cancellation* (SGLRTC) scheme [14, 4].

3 Data

The data used in this work is an interferometric stack comprising 32 Cosmo-SkyMed stripmap images acquired over the Matter Valley in Swiss Alps in the summers between 2008-2013. The acquisitions in winters are not considered to avoid temporal decorrelation due to snow cover. The region of interest (ROI) selected for tomographic analysis is as shown in Fig. 1 (outlined in red). The SAR image clearly shows the layover cast over the valley floor. The optical image from Google Earth shows a 3D perspective of the area. The height difference between the valley floor and the mountain top is on the order of a kilometer. We can see vegetation stretched over the slopes in near range. As to the one in far range, which casts the layover, we can observe some bare rocks on the mountainside which may exhibit temporally coherent scattering.

4 Results

PSI processing is performed on the full scene shown in Fig. 1 (top). The residue of the multiple linear regression fit of the unwrapped atmospheric phases against easting, northing and height, is shown in Fig. 2. It is shown here for each interferometric layer in the data stack for the PS identified in the interferometric processing over the full scene, and has been geocoded. Fig. 3 shows the sample variogram and a circular model fit for the example layer. The PS for which significant deformation is measured have not been included in the variogram analysis and regression-kriging. BF-based differential tomography, with updated atmospheric correction at each discrete point along the elevation profile, is applied. Single and double scatterers are detected in the ROI with SGLRTC, setting the detection thresholds at 0.48 [14, 4]. The detected scatterers are geocoded and projected in Google Earth, as shown in Fig. 4. The PS found in the ROI are also shown for comparison.
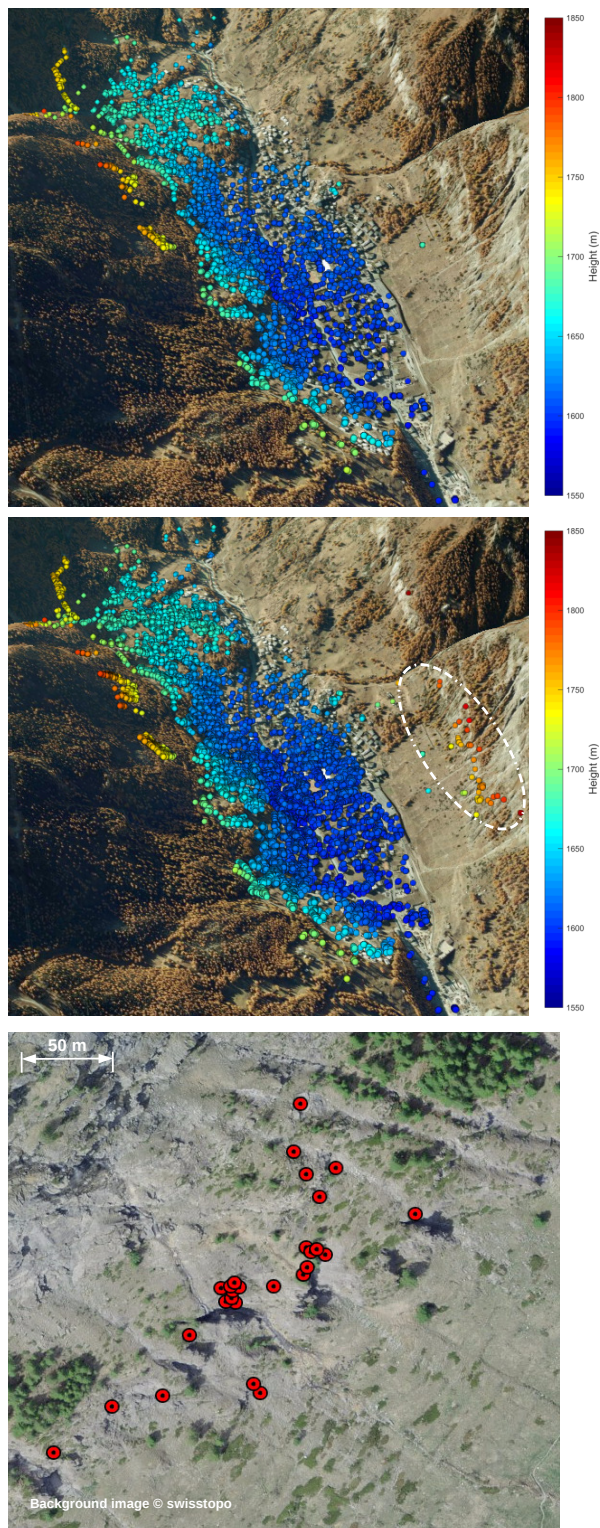

Figure 4: Geocoded scatterers. Top: PS identified in the prior PSI processing. Middle: Single and double scatterers obtained with tomography. Regression kriging-based height-dependent atmospheric corrections have been applied. The color-coding represents the estimated height. Enclosed in white boundary are the single scatterers obtained only with tomography around 230 m above the valley floor, only after applying the proposed regression-kriging based atmospheric corrections. Bottom: A zoom-in of the terrain along the mountainside where these scatterers are detected (courtesy Swisstopo).

4

5 Discussion & Outlook

It can be seen in Fig. 1 that the valley floor is partly covered with the layover cast by the adjoining mountain. A few PS are found even in the layover, representing those pixels where one among the other scattering contributions dominates the other. Nearly all of such PS are situated within the valley, and there is no coverage along the mountainside or the top, as can be seen in Fig. 4 (top). Since the PS distribution also represents the sampling of the 3D atmosphere that is subsequently interpolated with kriging, lack of PS at high altitudes is inopportune as it leads to high predication error variance. For the detection of single and double scatterers after atmospheric phase correction and tomographic inversion, the detection thresholds are set such that there are no obvious false alarms over decorrelated areas (e.g. forest) or detections at impossible locations (mid-air, below ground) after geocoding. A few single scatterers are detected on the mountainside around 230 m above the valley floor where no PS were found with the PSI processing, as highlighted in Fig. 4. They are detected on a vegetation-free rocky patch along the mountainside. It substantiates the usefulness of the kriging-based atmospheric estimations introduced in the paper. However, the overall gain in deformation sampling with layover separations remains limited as only a very few double scatterers are detected, which are mostly within the built-up area in the valley floor.

References

[1] R. Hanssen, *Radar interferometry: Data interpretation and error analysis*, vol. 2, Springer Science & Business Media, 2001.

[2] S. Tebaldini and A. Guarnieri, "On the role of phase stability in SAR multibaseline applications," *IEEE Trans. Geosci. Remote Sens.*, vol. 48, no. 7, pp. 2953–2966, July 2010.

[3] G. Fornaro, F. Lombardini, and F. Serafino, "Three-dimensional multipass SAR focusing: Experiments with long-term spaceborne data," *IEEE Trans. Geosci. Remote Sens.*, vol. 43, no. 4, pp. 702–714, Apr. 2005.

[4] M. Siddique, U. Wegmuller, I. Hajnsek, and O. Frey, "Single-Look SAR tomography as an add-on to PSI for improved deformation analysis in urban areas," *IEEE Trans. Geosci. Remote Sens.*, vol. 54, no. 10, pp. 6119–6137, Oct 2016.

[5] F. Lombardini, "Differential tomography: A new framework for SAR interferometry," *IEEE Trans. Geosci. Remote Sens.*, vol. 43, no. 1, pp. 37–44, 2005.

[6] G. Fornaro, A. Pauciullo, D. Reale, and S. Verde, "Multilook SAR tomography for 3-D reconstruction and monitoring of single structures applied to COSMO-SKYMED data," *IEEE J. Sel. Topics Appl. Earth Observ. in Remote Sens*, vol. 7, no. 7, pp. 2776–2785, July 2014.

[7] C. Werner, U. Wegmüller, T. Strozzi, and A. Wiesmann, "Interferometric point target analysis for deformation mapping," in *Proc. IEEE Int. Geosci. Remote Sens. Symp.*, 2003, pp. 4362–4364.

[8] O. Frey, M. Santoro, C. Werner, and U. Wegmuller, "DEM-based SAR pixel area estimation for enhanced geocoding refinement and radiometric normalization," *IEEE Geosci. Remote Sens. Lett.*, vol. 10, no. 1, pp. 48–52, Jan. 2013.

[9] T. Strozzi, R. Caduff, U Wegmuller, H. Raetzo, and M. Hauser, "Widespread surface subsidence measured with satellite SAR interferometry in the Swiss alpine range associated with the construction of the Gotthard Base Tunnel," *Remote Sens. of Environm.*, vol. 190, pp. 1 – 12, 2017.

[10] Rubén Iglesias, Xavier Fabregas, Albert Aguasca, Jordi J Mallorqui, Carlos López-Martínez, Josep A Gili, and Jordi Corominas, "Atmospheric phase screen compensation in ground-based SAR with a multiple-regression model over mountainous regions," *IEEE Trans. Geosci. Remote Sens.*, vol. 52, no. 5, pp. 2436–2449, 2014.

[11] M. Siddique, I. Hajnsek, and O. Frey, "A case study on the use of differential SAR tomography for measuring deformation in layover areas in rugged alpine terrain," in *Proc. IEEE Int. Geosci. Remote Sens. Symp.*, 2017.

[12] Z. Hu, J. Mallorqui, G. Centolanza, and J. Duro, "Atmospheric artefacts mitigation with a covariance weighted linear model over mountainous regions," in *ESA 10th FRINGE Workshop*, 2017.

[13] R. Bivand, E. Pebesma, and V. Gomez-Rubio, *Applied spatial data analysis with R*, vol. 747248717, Springer, 2008.

[14] A. Pauciullo, D. Reale, A. De Maio, and G. Fornaro, "Detection of double scatterers in SAR tomography," *IEEE Trans. Geosci. Remote Sens.*, vol. 50, no. 9, pp. 3567–3586, 2012.